machines

Article

Numerical Simulation and Analysis of the Flow Characteristics of the Roof-Attached Vortex (RAV) in a Closed Pump Sump

Bowen Zhang [1], Li Cheng [1,*], Minghu Zhu [2], Weixuan Jiao [1] and Di Zhang [1]

[1] College of Hydraulic Science and Engineering, Yangzhou University, Yangzhou 225009, China; dx120190073@yzu.edu.cn (B.Z.); jiaowx@yzu.edu.cn (W.J.); dx120180054@yzu.edu.cn (D.Z.)
[2] Dafeng District Water Resources Bureau, Yancheng 224100, China; minghuzhu@126.com
* Correspondence: chengli@yzu.edu.cn

Abstract: Unsteady numerical simulation and visual experiment are used to reveal the formation mechanism of the roof-attached vortex (RAV) on the roof of the closed sump of a pumping station. The results show that RAVs mainly occur between the pump device and the rear wall of the closed sump. In the 10th period of impeller rotation, there are 2 RAVs at the roof. V1 (Vortex 1 in numerical simulation) is located directly behind the water pump unit, and V2 (Vortex 2 in numerical simulation) is close to the right wall. Significantly, the vorticity intensity at the V1 vortex core increases with the rotation of the impeller. $V_{test}1$ (Vortex 1 in test) and $V_{test}2$ (Vortex 2 in test) are two RAVs observed in the experiment, which are highly consistent with the unsteady numerical simulation V1 and V2. Comparing the vorticity intensity of the roof, rear wall, and sidewall, it can be seen that the maximum vorticity intensity on the roof is more significant than that on the rear wall and both sides of the wall. The roof is more likely to induce vortex. When the RAVs on the roof occur, the pressure in the middle of the bell mouth is lower than that on the sidewall, and the velocity is higher. At 2/5 T, the blade is in the low-pressure zone. The velocity distribution uniformity and velocity weighted average angle at the bell mouth also decreased. The RAVs enter the pump after being generated, which is the most harmful to the safe and stable operation of the pump. The study can provide theoretical guidance for the optimal design of the closed sump.

Keywords: computational fluid dynamics; mechanical pump; closed sump; roof-attached vortex; vorticity distribution

check for updates

Citation: Zhang, B.; Cheng, L.; Zhu, M.; Jiao, W.; Zhang, D. Numerical Simulation and Analysis of the Flow Characteristics of the Roof-Attached Vortex (RAV) in a Closed Pump Sump. *Machines* **2022**, *10*, 209. https://doi.org/10.3390/machines10030209

Academic Editor: Ahmed Abu-Siada

Received: 1 March 2022
Accepted: 14 March 2022
Published: 15 March 2022

Publisher's Note: MDPI stays neutral with regard to jurisdictional claims in published maps and institutional affiliations.

Copyright: © 2022 by the authors. Licensee MDPI, Basel, Switzerland. This article is an open access article distributed under the terms and conditions of the Creative Commons Attribution (CC BY) license (https://creativecommons.org/licenses/by/4.0/).

1. Introduction

The pumping station is an essential infrastructure in urban water supply and drainage. The sump of the pumping station is a crucial hydraulic structure in hydraulic engineering. Vortices in the pump sump are the main adverse flow patterns endangering the safe and stable operation of the pumping station. The open sump (Figure 1a) is often prone to form surface vortices [1–4]. With the transformation of pumping stations and the development of energy conservation worldwide, the open sump is undergoing a closed transformation. A concrete top plate is set at the position of the pump beam to close the open sump. By eliminating the structures in the sump, such as the pump beam and maintenance platform, the interference of free water surface and structures on the flow in the sump is reduced, and a closed sump (Figure 1b) is formed. The vortex in the sump is the main lousy flow pattern endangering the safe and stable operation of the pump station. When the vortex occurs, the pressure of the water body near the vortex decreases sharply, and the gas in the water body precipitates. When the gas accumulates to a certain extent, the vortex will carry air to form a vortex belt into the impeller. The pump unit will produce violent vibrations and even fail to operate.

Although the free surface vortex has been effectively prevented and controlled, it induces a new vortex band at the roof [5]. This vortex band is called roof-attached vortex

(RAV). RAV is generated under the roof and is not easy to detect. The flow mechanism and influencing factors of RAV are complex, challenging to prevent and control. More seriously, when the RAV is generated, the flow pulsation in the sump will be intensified. This will lead to the vibration of the pumping station and its nearby facilities and endanger the operation safety of the pumping station.

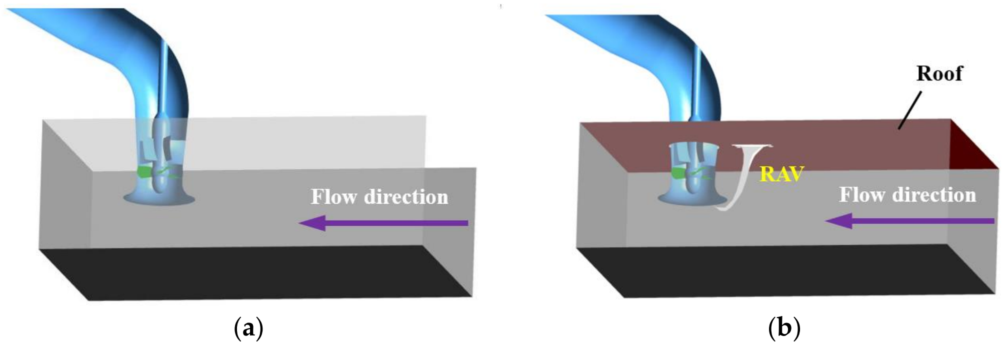

Figure 1. Different types of pump sump. (**a**) open sump. (**b**) closed sump.

The vortex in the pump sump has always been a critical research problem in hydrodynamics [6,7]. The vortex formation is fundamentally due to the existence of a vorticity source. Fluid micro clusters are affected by the mass force and surface force. If the mass force cannot be expressed as the gradient of a scalar function, it will cause the rotational motion of the fluid micro cluster and lead to the existence of a vorticity source [8]. Hamed Sarkardeh [9] established an analytical model of vertical inlet vortex. By assuming that the vortex streamline is spiral, he solved the continuity and momentum equations in the vortex basin. Song et al. [10–12] carried out a lot of research on the attached-bottom vortex (ABV) of the open pump sump. To explore the formation mechanism of vortex characteristics, volumetric three-component velocimetry measurements (V3V) are used to measure the flow field below the suction inlet of an axial flow pump. The evolution process of the floor-attached vortex (FAV) can be divided into five stages: initiation, development, continuation, collapse, and disappearance. Kang et al. [13] conducted a preliminary and experimental study on the behavior of suction vortices, including cavitation, free vortices, and subsurface vortices in a multi-sump system under different velocities and water level conditions. Pan et al. [14] used the large eddy simulation method to simulate the flow and related vortices in the pump sump. Ayham Amin et al. [15] conducted numerical and experimental analysis on the rectangular pump sump to predict the vortex angle and the formation of a free surface vortex. Hyung Jun [16], Arocena [17], Behrouz [18], Ahmad [19], Echamiriavez [20] conducted experimental research and numerical simulation on the formation of surface vortices and underwater vortices in the sump. Cheng et al. [21], Jiao et al. [22] carried out a series of studies on vortex elimination measures. Rajendran [23] used two-dimensional particle image velocimetry (PIV)to test the flow field in the sump. The instantaneous and time-average velocity fields and vorticity fields at different positions are obtained. Constantinescu [24,25] calculated the flow field when the critical flow characteristics appeared in the sump. Choi et al. [26] used a multi-pump sump model with seven pump intakes and a single-intake pump sump for investigation. The effectiveness of an anti-submerged vortex device (AVD) for suppressing the vortex occurrence in a single pump intake and a multi-intake pump sump model has been examined by experiment and numerical analysis methods. Okamura [27] used the slice laser visualization method to obtain the vortex distribution in the inlet pool model. The vorticity distribution in the same physical model is obtained by PIV technology.

Although much research has been done on the vortex in the open pump sump, there is still no in-depth study on the RAV in the closed sump. There are two main methods to study RAV, model test, and numerical simulation. Based on computational fluid dynamics, the unsteady numerical simulation of RAV in a closed sump is carried out in this study.

We predict the location and relative intensity of RAV. Nowadays, the closed sump is widely used in the primary physical isolation inlet sump of the sewage treatment plant, underground deep pump station, and other necessary energy application fields. Therefore, the investigation has essential application value in many industries and areas.

2. Research Model and Numerical Calculation

The computational fluid dynamics (CFD) numerical simulation method has been widely used in many fields such as water conservancy, energy, and environment. In this paper, the fluid analysis software ANSYS™ CFX software is used for the unsteady numerical calculation of RAV.

2.1. Governing Equation

The three-dimensional incompressible viscous flow is described based on the mass and linear momentum balance equations. The medium conveyed by the pump device is water. The water density change in the flow process can be ignored to be regarded as an incompressible fluid. The expression of the N-S equation in a rectangular coordinate system is as follows [28]

$$\frac{\partial u_i}{\partial x_i} = 0, \tag{1}$$

$$\frac{\partial}{\partial t}(\rho u_i) + \frac{\partial}{\partial x_j}(\rho u_i u_j) = -\frac{\partial p}{\partial x_i} + \frac{\partial \tau_{ij}}{\partial x_j} + \rho g_i + F_i. \tag{2}$$

where, ρ represents water density; u_i, u_j represent the fluid's velocity in the directions of component i and j; t represents time; p represents pressure; F_i represents external source term; x_i, x_j are three-dimensional coordinate components. τ_{ij} is the stress tensor, and its expression is as follows

$$\tau_{ij} = \left[\mu\left(\frac{\partial u_i}{\partial x_j} + \frac{\partial u_j}{\partial x_i}\right)\right] - \frac{2}{3}\mu\delta_{ij}\frac{\partial u_i}{\partial x_i}. \tag{3}$$

where, μ represents dynamic viscosity; δ_{ij} is the Kronecker delta (when $I = j$, $\delta_{ij} = 1$; When $I \neq j$, $\delta_{ij} = 1$). If the influence of gravity is ignored, the momentum equation is as follows

$$\frac{\partial}{\partial t}(\rho u_i) + \frac{\partial}{\partial x_j}(\rho u_i u_j) = F_i - \frac{\partial p}{\partial x_i} + \frac{\partial}{\partial x_j}\left[\mu\left(\frac{\partial u_i}{\partial x_j} + \frac{\partial u_j}{\partial x_j}\right)\right]. \tag{4}$$

2.2. Research Model

The whole simulation model includes a closed sump, impeller, guide vane, inlet tank, outlet pipe, and pressure outlet tank. Table 1 shows the basic parameters of the hydraulic model of the axial flow pump.

Table 1. Basic parameters of the hydraulic model of the axial flow pump.

Parameters	Value
Impeller diameter	D = 120 mm
Tip clearance	0.15 mm
The ratio of hub and shroud	0.36
Bell mouth diameter	D_L = 190 mm
Number of pump blades	Z_1 = 3
Impeller speed	n = 2400 r/min
Number of guide vanes	Z_2 = 5

According to the practical application of the closed sump, the calculation model of the closed sump is constructed (Figure 2).

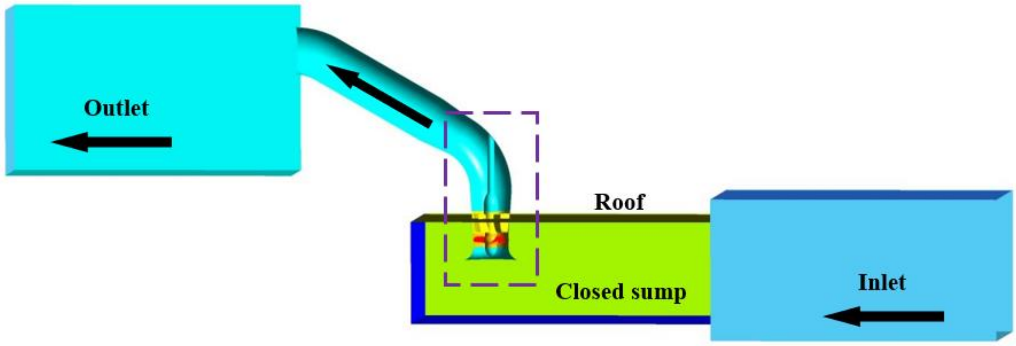

(**a**)

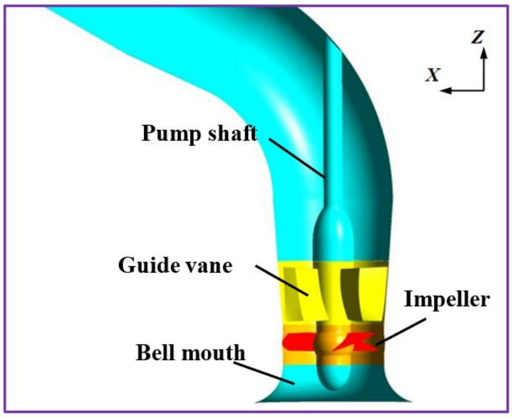

(**b**)

Figure 2. Simulation domain of the closed sump. (**a**) Integral calculation model of the closed sump. (**b**) Pump section model.

As shown in Figure 3, the geometric parameters of the calculation model of the closed sump are as follows: sump length $L_S = 5.37\ D_L$, sump width $B_S = 3.58\ D_L$, roof height $H_d = 1.51\ D_L$, suspended height $C = 1.01\ D_L$, and roof inundation depth $H_S = 1.03\ D_L$.

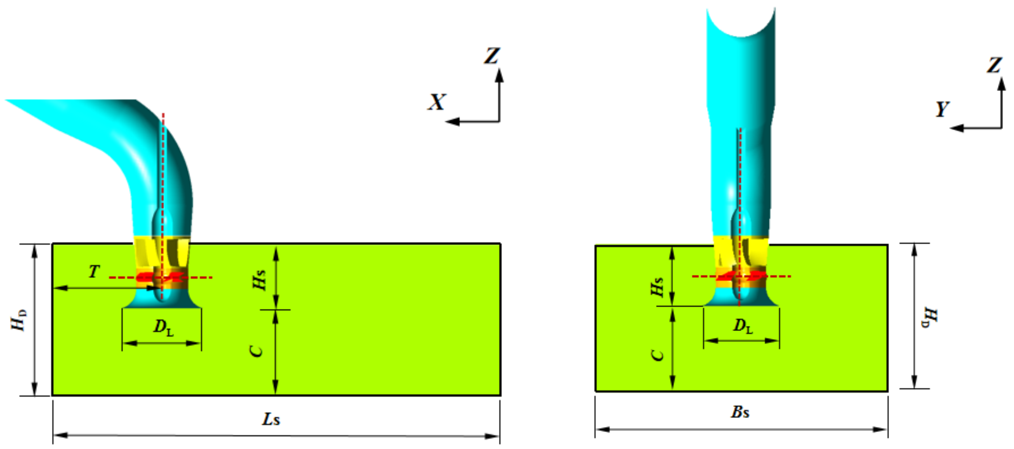

(**a**) (**b**)

Figure 3. Schematic diagram of geometric parameters of the closed sump. (**a**) Front view. (**b**) Side view.

2.3. Grid Study

In numerical calculation, the number and size of grids will affect the reliability of calculation results. Theoretically, with the increase of grid density, the discretization error of calculation results decreases. The calculation results will be more accurate. Based on the ICEM CFD mesh generation module, a block strategy is adopted to divide the structured mesh of impeller, guide vane, closed sump, and other parts (Figure 4). The quality of the generated grid is good, and the face angle range is between 20 and 160 degrees. To obtain more accurate results, the grid in the area around the blade is encrypted, and the $y+$ value is between 10 and 100 in the whole calculation domain.

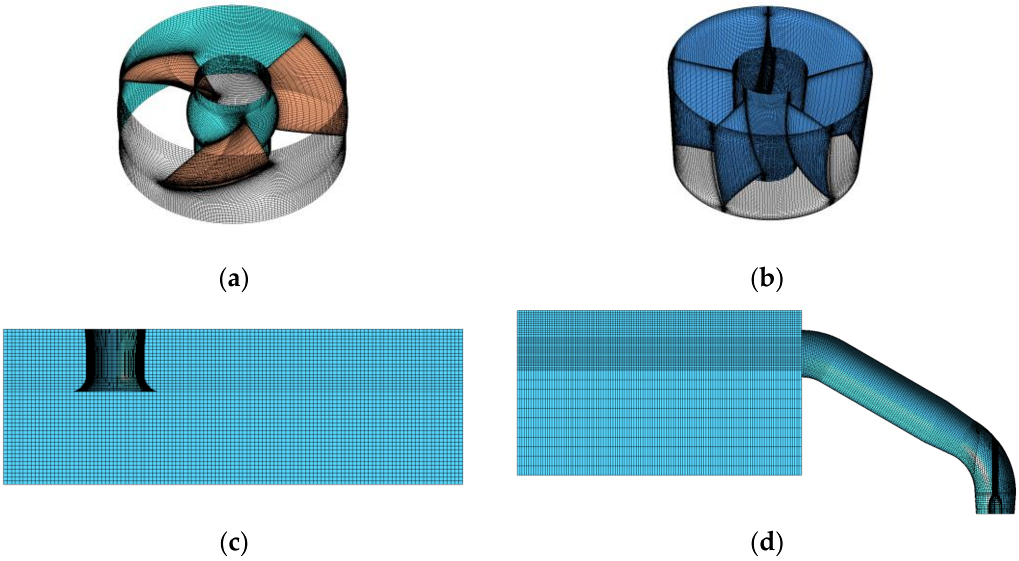

Figure 4. Grid generation. (**a**) Impeller. (**b**) Guide vane. (**c**) Closed sump. (**d**) Outlet pipe and pressure tank.

We mainly checked the grid independence of the pump section of the closed sump model. Based on the entire grid topology of impeller and guide vane, four grids with different densities are obtained through overall encryption. The specific number of grid cells is shown in Table 2. It can be seen from Table 2 when the number of grid elements is small, the pump section head predicted by numerical calculation is high. When the number of grid elements is more than 300,000, the change of pump head predicted by numerical computation is small. The number of grid cells in the pump section we finally adopted is 608,565.

Table 2. Sensitivity analysis of pump section mesh.

Number	Number of Grid Cells	Pump Section Head/m
1	128,265	2.39
2	288,222	2.37
3	608,565	2.37
4	1,087,590	2.37

2.4. Turbulence Model

The turbulence model has an important influence on the vortex simulation in the sump [29,30]. Different turbulence models also have different prediction accuracy of vortex location and intensity. Five vortex viscosity models in Reynolds averaged Navier–Stokes equations were analyzed and compared. The turbulence model includes Standard k-ε Model, Renormalization Group (RNG k-ε) Model, Standard k-ω Model, Shear Stress Transport (SST) k-ω Model and Baseline (BSL) k-ω Model [31]. The Standard k-ε Model is introduced turbulent dissipation rate ε equation, combined with the rough kinetic energy k equation to form a two-equation model. The Standard k-ε Model has the advantages of simplicity, stability, reasonable calculation accuracy, and wide application range.

Figure 5 shows the relative errors between the numerical calculation results of the head and efficiency of each turbulence model and the experimental values. The comparison results show that the relative error rate between the numerical simulation and the experimental value of head is 0.23% under Standard k-ε Model is 0.23%. Furthermore, the relative error rate between the numerical simulation and experimental efficiency values is 0.25%. The numerical simulation values are in good agreement with the experimental values. Therefore, we choose Standard k-ε Model as the simulation model.

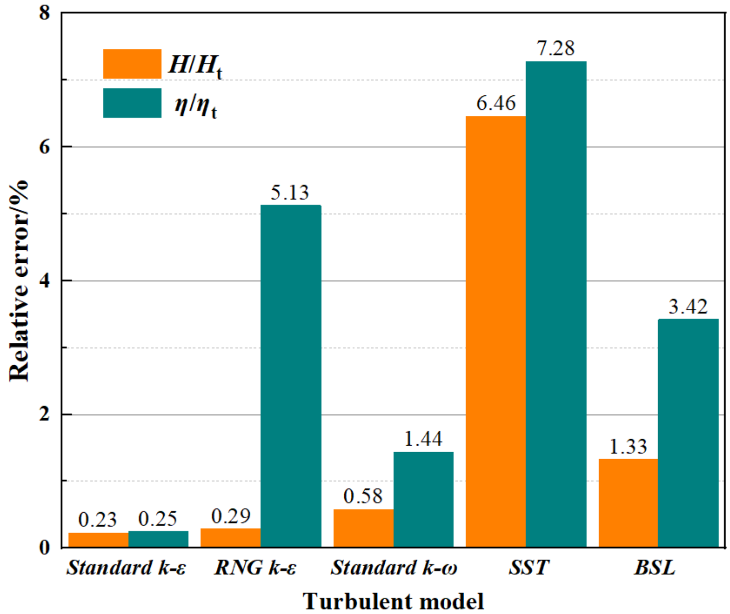

Figure 5. Comparison of relative error values of turbulence models.

2.5. Calculation Parameter Settings

The time step of unsteady simulation has an essential influence on the results. The total calculation time length was set to 0.25 s and each time step of the unsteady calculation is 0.0025 s. Unsteady simulation is carried out every 36 degrees of impeller rotation. The total calculation period (T) is ten impeller rotation periods. The results of the steady calculation are used as the initial conditions of unsteady analysis. The calculation parameter settings of unsteady calculation are shown in Table 3.

Table 3. Calculation parameter settings of unsteady numerical simulation.

Main Parameters	CFX Settings
Flow hypothesis	Incompressible
Simulation type	Transient
time step	0.0025 s
Total time	0.25 s
Inlet boundary conditions	Mass flow, Q = 36.3 kg/s
Outlet boundary conditions	1 atm
Rotational speed	2400 rev/min
Static-static interface	GGI
Dynamic-static interface	Transient Rotor Stator
Wall condition	Non-slip
Wall function	Scalable wall function
Convergence accuracy	10^{-5}

3. Results

3.1. Distribution Characteristics of RAV

Although people can judge the existence of a vortex by image and intuition in simple flow, the vortex has not been clearly defined in mathematics. To objectively evaluate the presence of vortex in the experiment and numerical simulation, it is necessary to have a mathematical criterion for vortex. And this criterion can remain unchanged in Galileo's transformation. The orientation of the vortex axis does not change with the transformation of the coordinate system.

In order to accurately capture and identify the vortex structure of the flow field, there are two mainstream vortex identification criterions, Q criterion and Δ criterion. The first is the Q criterion proposed by Hunt [32]. Q is the second Galilean invariant of the velocity gradient tensor. The region with $Q > 0$ is defined as a vortex. The critical point is that the vorticity of the fluid plays a leading role in the vortex compared with the strain rate. The Q criterion reveals the equilibrium relationship between vortex deformation and rotation in the flow field. It is considered that there is rotational flow in the region where $Q > 0$, but sometimes the condition that the pressure in the vortex region is less than the ambient pressure needs to be met.

Based on the second-order tensor characteristics, the characteristic equation of local velocity gradient tensor ∇V of an incompressible fluid is as follows

$$S_{ij} = \frac{1}{2}\left(\frac{\partial u_i}{\partial x_j} - \frac{\partial u_j}{\partial x_i}\right), \tag{5}$$

$$\Omega_{ij} = \frac{1}{2}\left(\frac{\partial u_i}{\partial x_i} + \frac{\partial u_j}{\partial x_i}\right), \tag{6}$$

$$Q = \frac{1}{2}\left(\left|\left|\Omega_{ij}\right|\right|^2 - \left|\left|S_{ij}\right|\right|^2\right). \tag{7}$$

Here, S_{ij} is the strain rate tensor, Ω_{ij} is the vorticity tensor, $|| \, ||$ is the Frobenius parametrization of the matrix. The simplification to Q in three-dimensional cartesian coordinates is as follows

$$Q = -\frac{1}{2}\left(\left(\frac{\partial u}{\partial x}\right)^2 + \left(\frac{\partial v}{\partial y}\right)^2 + \left(\frac{\partial w}{\partial z}\right)^2\right) - \frac{\partial u}{\partial y}\frac{\partial v}{\partial x} - \frac{\partial u}{\partial z}\frac{\partial w}{\partial x} - \frac{\partial v}{\partial z}\frac{\partial w}{\partial y}. \tag{8}$$

Here, u, v, and w are the velocities in the x, y, and z directions, respectively.

The second is the Δ criterion proposed by Dallmann [33]. For incompressible fluids, the characteristic equation of the velocity gradient tensor and Δ are as follows [34]

$$\lambda^3 + P\lambda^2 + Q\lambda + R = 0, \tag{9}$$

$$\Delta = \left(\widetilde{Q}/3\right)^2 + \left(\widetilde{R}/2\right)^2. \tag{10}$$

Here, $\widetilde{Q} = Q - P^2/3$, $\widetilde{R} = R + \left(2P^3\right)/27 - PQ/3$.

Chong et al. [35] defined a vortex as a region where a couple of complex conjugate eigenvalues exists for the velocity gradient tensor ∇V, based on the critical point theory. When ∇V has a couple of complex conjugate eigenroots, the representative instantaneous flow has a closed or spiral form. The Δ criterion will determine where Q criterion is not vortex area as vortex area. To determine the vortex in the three-dimensional region of the closed pump sump, we used the Q criterion. The vortex on the two-dimensional wall's vorticity component (W_{i}) perpendicular to the wall was used.

The 10th periodic data of the unsteady state calculation were selected to analyze the RAV characteristics in the closed sump. As shown in Figure 6, there are 2 RAVs (V1 and V2) around the roof at the time T. V1 is directly behind the pump unit, and V2 is close to the right wall. At the same level of Q, the vortex strength of V1 is more significant than V2.

Figure 7 shows the streamline and vorticity intensity in the roof area at T. It can be seen from Figure 7 that the vorticity intensity of V1 is the highest and the vorticity range of V2 is the widest.

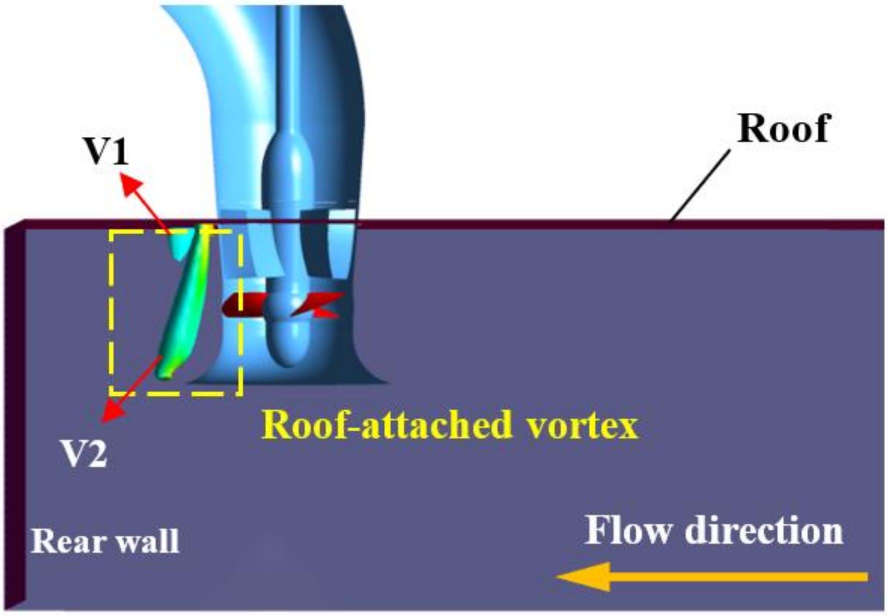

Figure 6. Roof-attached vortex (RAV) in the closed sump at the time T (Q = 5.02 s^{-2}).

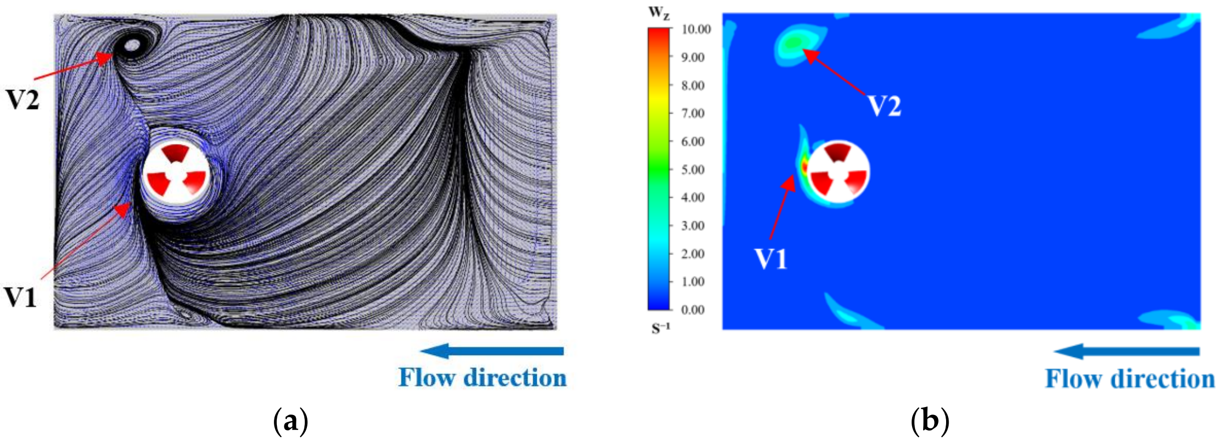

Figure 7. Streamline and vorticity intensity distribution near the roof at time T. (**a**) Streamline. (**b**) Vorticity.

In order to verify the accuracy of numerical simulation, a cyclic experimental system of transparent closed sump model was established. As shown in Figure 8, the loop length of the whole experimental device is 12 m. The length of the closed sump model is 3.3 m, and the model includes inlet tank, closed sump, a pump device, and pressure outlet tank. The length of the circulating test system is 8.7 m, and the system includes an auxiliary pump, electromagnetic flowmeter, and connecting pipe. To facilitate the observation of experimental phenomena, a closed sump body is made of a transparent plexiglass plate.

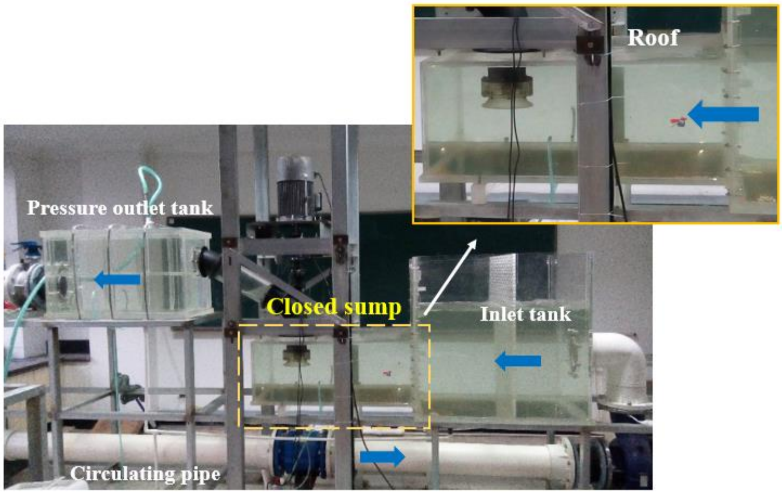

Figure 8. Circulating experimental device of the closed sump model.

The geometric parameters of the closed sump experimental model are as follows: sump length L_S = 5.37 D_L, sump width B_S = 3.58 D_L, roof height H_d = 1.51 D_L, suspended height C = 1.01 D_L, and roof inundation depth H_S = 1.03 D_L. These are consistent with the parameters of CFD numerical simulation. The experimental pump device is a metal component, mainly bell mouth, impeller, guide vane, 60° elbow, outlet pipe, and shafting components.

From Figure 9, it can be seen that $V_{test}1$ (Vortex 1 in test) and $V_{test}2$ (Vortex 2 in test) observed in the experiment agree well with the numerical simulation results. The position of $V_{test}2$ is very consistent with that of V2, while the position of $V_{test}1$ is slightly different from that of V1. This is because the numerical simulation simplifies the wall details of the pump unit to facilitate high-quality meshing and obtain more accurate results. $V_{test}1$ and $V_{test}2$ are vortices entering the pump, which greatly influence the safe and stable operation of the pump unit. It is consistent with the vorticity intensity distributions of V1 and V2 obtained by numerical calculation.

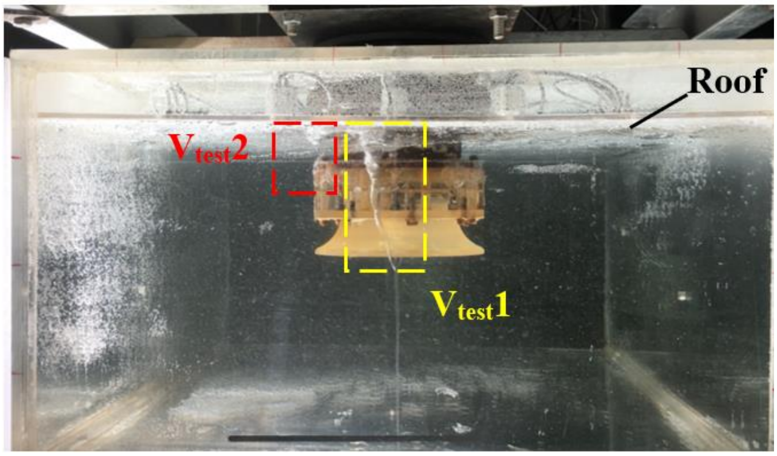

Figure 9. Experimental phenomena of RAV (side view).

Thus, the numerical simulation based on the Standard *k-ε* Model can accurately predict the location and relative vorticity intensity of the RAV in the closed sump. RAV mainly occurs between the pump device and the rear wall in the closed sump. The RAV directly behind the pump device will enter the pump, which is the most harmful to the safe and stable operation of the pump system. The distribution of RAV along both sides of the flow direction is asymmetric.

The tangential velocity distribution of the vortex is an important feature to distinguish the vortex flow characteristics. As shown in Figure 10, we take the velocity distribution of four cross-sections at the location where the vortex occurs on the rear wall of the closed sump for analysis—taking the inlet flow rate (V_{in}) and impeller radius (D) as characteristic quantities. Regularize the tangential velocity, and the result is shown in Figure 11. The tangential velocity of the vortex first increases and then decreases with the increase of radius. It belongs to the Rankine vortex, composed of the free and forced vortex. The radius corresponding to the maximum tangential velocity is the vortex core radius. And the tangential velocity distribution law is consistent under different axial depths.

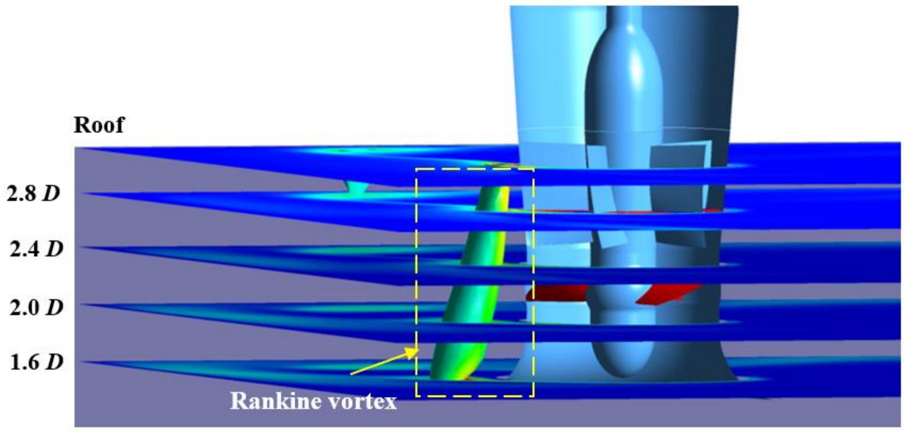

Figure 10. Rankine vortex in the closed sump.

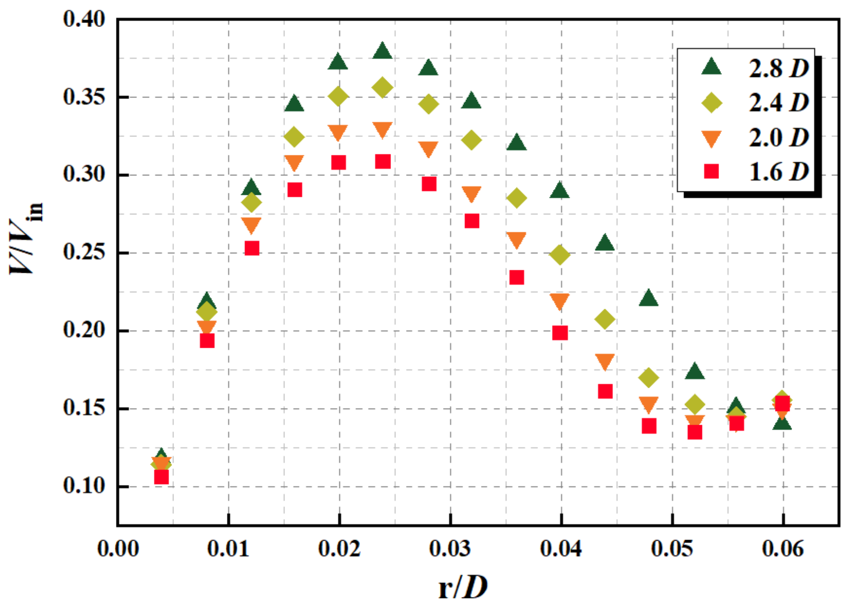

Figure 11. Variation of tangential velocity with radius at different depths.

3.2. Distribution Characteristics of the Wall Vorticity Field

Figure 12 shows the vorticity field distribution near the roof in one rotation period of the impeller. Figure 13 shows the streamline near the roof at different time points. It can be seen from the figure that the distribution of the vorticity field near the roof is the same at other time points. The positions of V1 and V2 do not change significantly within one period of impeller rotation.

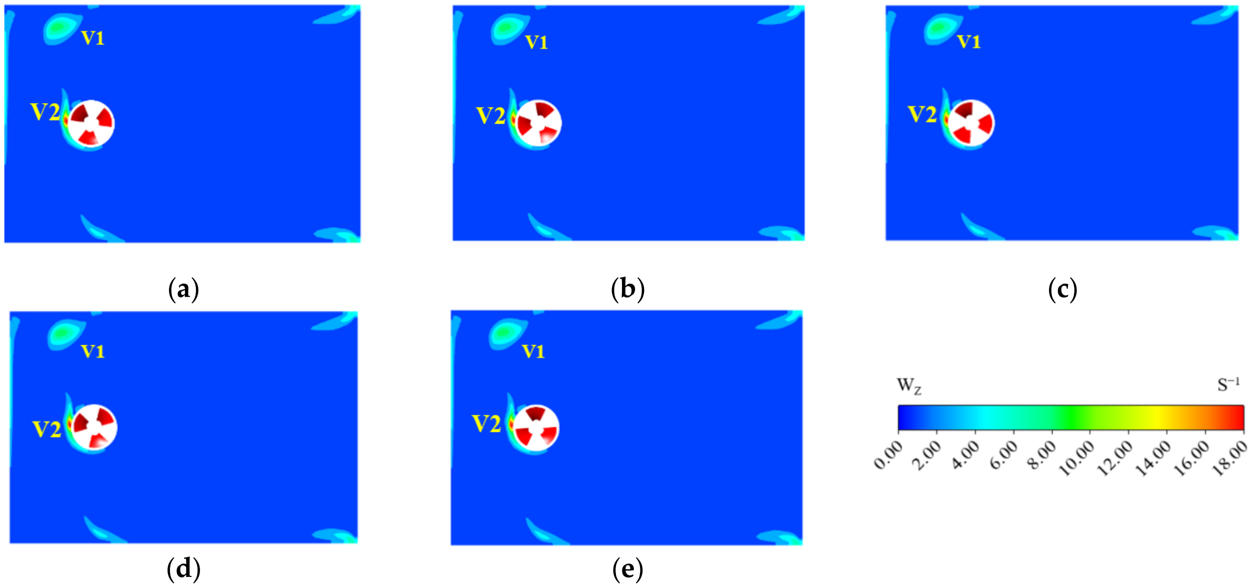

Figure 12. Vorticity field distribution near the roof at different time points. (**a**) 1/5T, (**b**) 2/5T, (**c**) 3/5T, (**d**) 4/5T, (**e**) T.

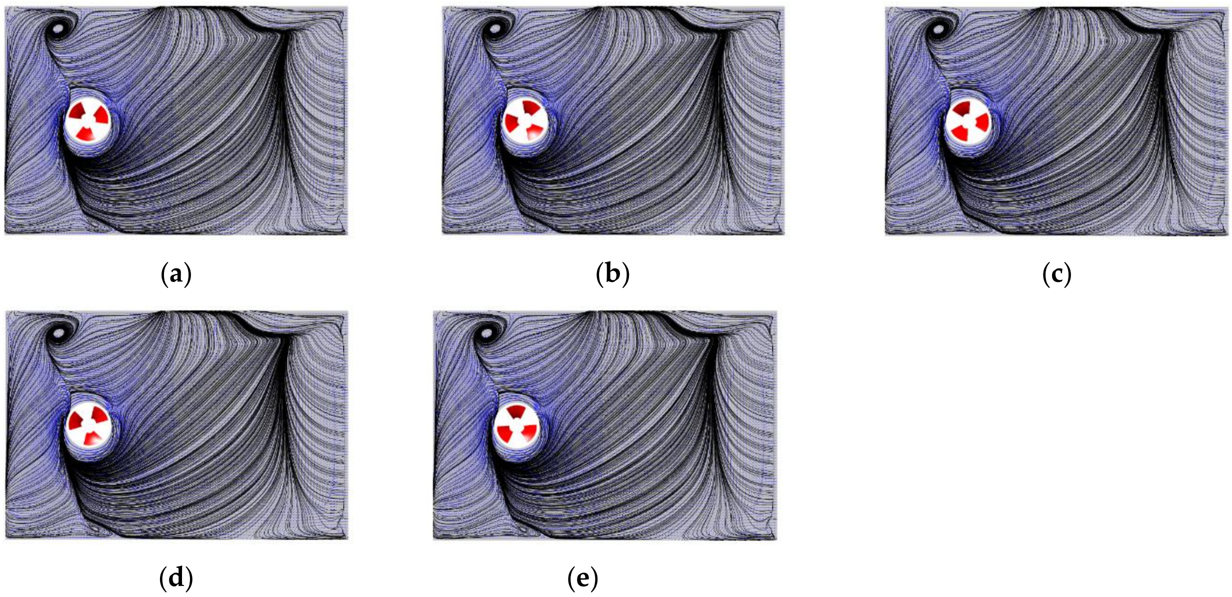

Figure 13. Streamline near the roof at different time points. (**a**) 1/5T, (**b**) 2/5T, (**c**) 3/5T, (**d**) 4/5T, (**e**) T.

Therefore, the distribution characteristics of the vorticity field at the roof predicted by numerical simulation can remain relatively stable in one impeller rotation period. With the rotation of the impeller, the vorticity intensity at the vortex core continues to converge (Figure 14). In the experimental observation, there is a precursory stage in the occurrence of RAV. The tiny bubbles precipitated or generated in the water flow will converge in the corresponding vortex generation area in the precursory location. This is the continuous generation and convergence of small-scale vortices. When the energy of the vortex reaches a certain degree, the large-scale vortex will be generated. Unsteady numerical simulation can accurately predict the location and intensity of RAV on a large scale. However, due to the limitations of grid size and turbulence model, it cannot capture the formation and development of small-scale vortices.

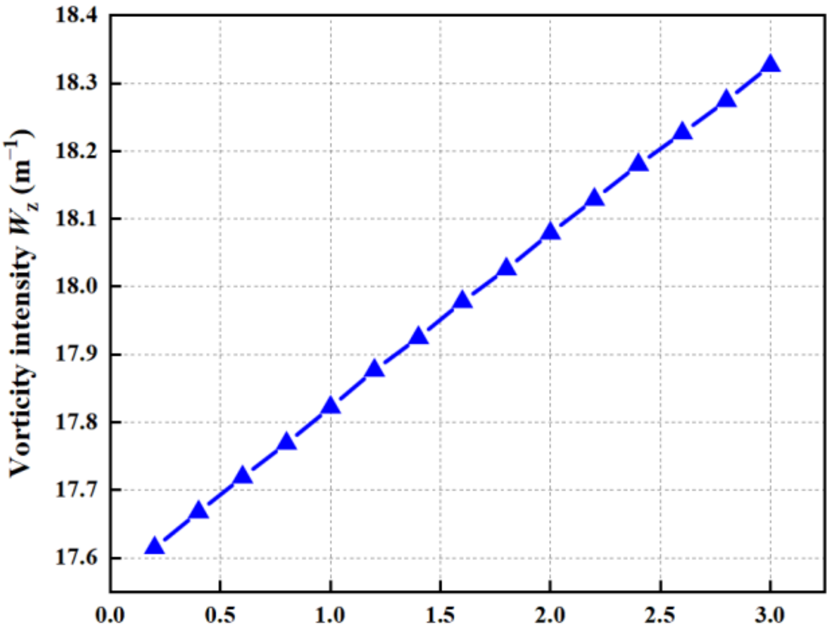

Figure 14. Vorticity intensity of V1 vortex core in 3 impeller rotation periods.

To analyze the vorticity field distribution of RAV along the axial direction, five sections (S1~S5) are taken along the axial direction in the closed inlet tank. As shown in Figure 15, S1 is the roof's surface, S3 is the center surface of the impeller, and S5 is the inlet surface of the bell mouth. As shown in Figure 16, take the vorticity field distribution of section S1~S5 at time T. It can be seen from the figure that with the increase of the axial distance from the roof, the area of V1 gradually increases and the vorticity intensity at the vortex core decreases. In addition, the position of V1 is not attached to the wall of the pump device. In sections S2–S4, the vortex V1 deviates from the water pump device, and in section S5, V1 is attached to the bell mouth of the pump device. The position of V2 gradually approaches the bell mouth with the increase of axial distance. In section S5, the bottom of V1 is attached to the bell mouth. The numerical simulation results are consistent with the experimental phenomena.

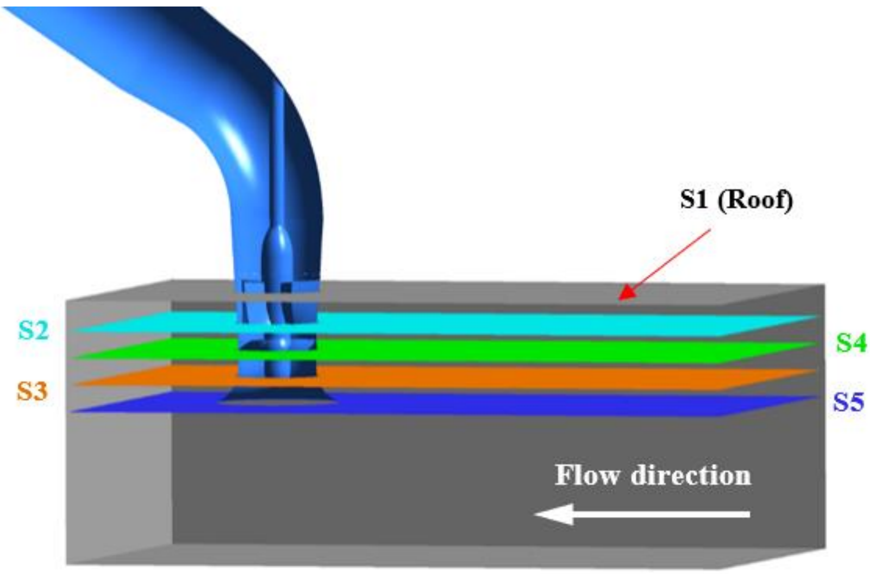

Figure 15. Five axial section positions.

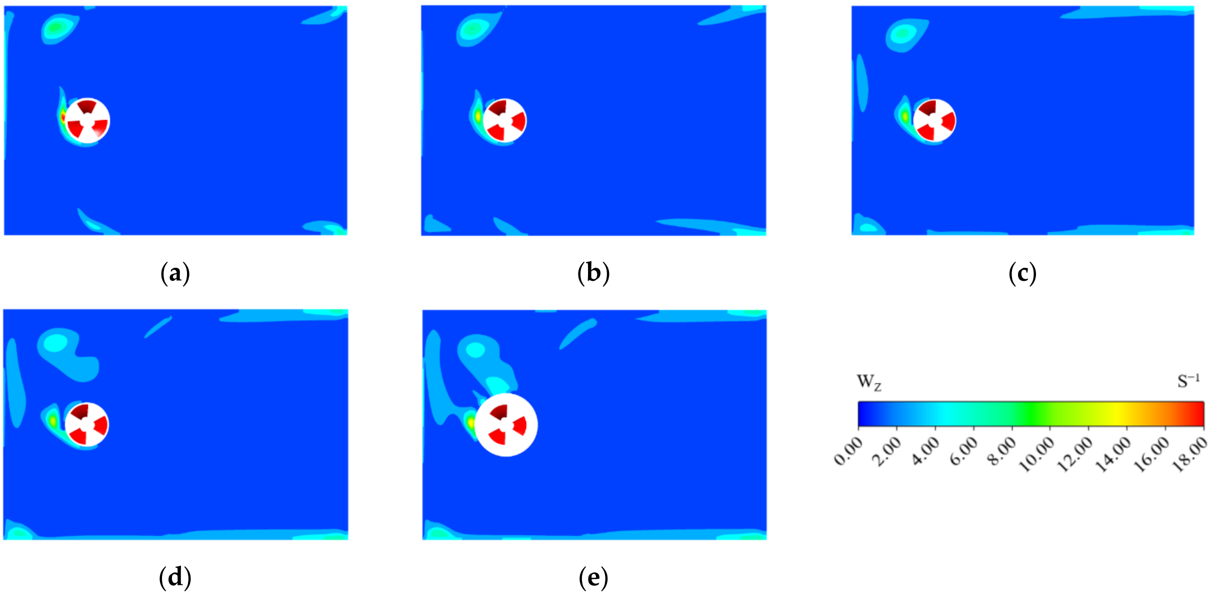

Figure 16. Vorticity intensity distribution at different sections (T). (**a**) S1. (**b**) S2. (**c**) S3. (**d**) S4. (**e**) S5.

The vorticity distribution on the rear wall and sidewalls of the closed sump does not change significantly in one rotation cycle of the impeller. Figures 17 and 18 respectively show the streamline and vorticity intensity distribution on the rear and sidewalls at time T. It can be seen from the figure that the vorticity on the rear wall region is concentrated at the right wall. There are two symmetrical vortices near the rear wall and the sidewalls. On the right wall of the sump, there are vortices near the roof and the water inlet.

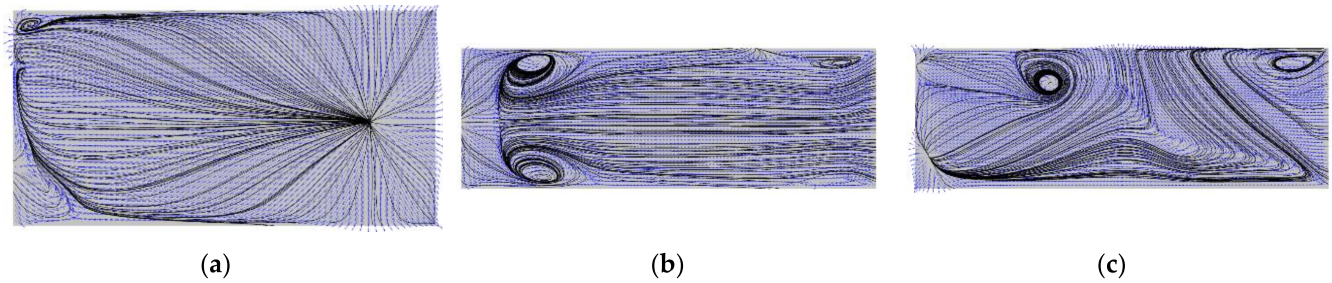

Figure 17. Streamline near the rear wall and sidewalls. (**a**) Rear wall region. (**b**) Left wall region. (**c**) Right wall region.

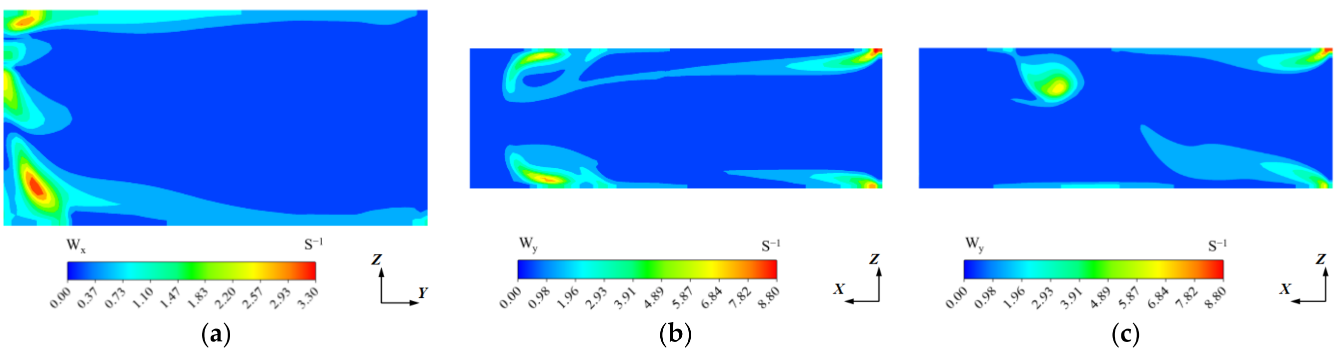

Figure 18. Vorticity intensity distribution near the rear wall and sidewalls. (**a**) Rear wall region. (**b**) Left wall region. (**c**) Right wall region.

As shown in Figure 19, the vorticity intensity of the roof, rear wall, and sidewalls was compared. It can be seen from the figure that the maximum vorticity intensity on the roof is greater than that on the rear wall and both sides of the wall. In other words, the roof is more likely to induce vortex.

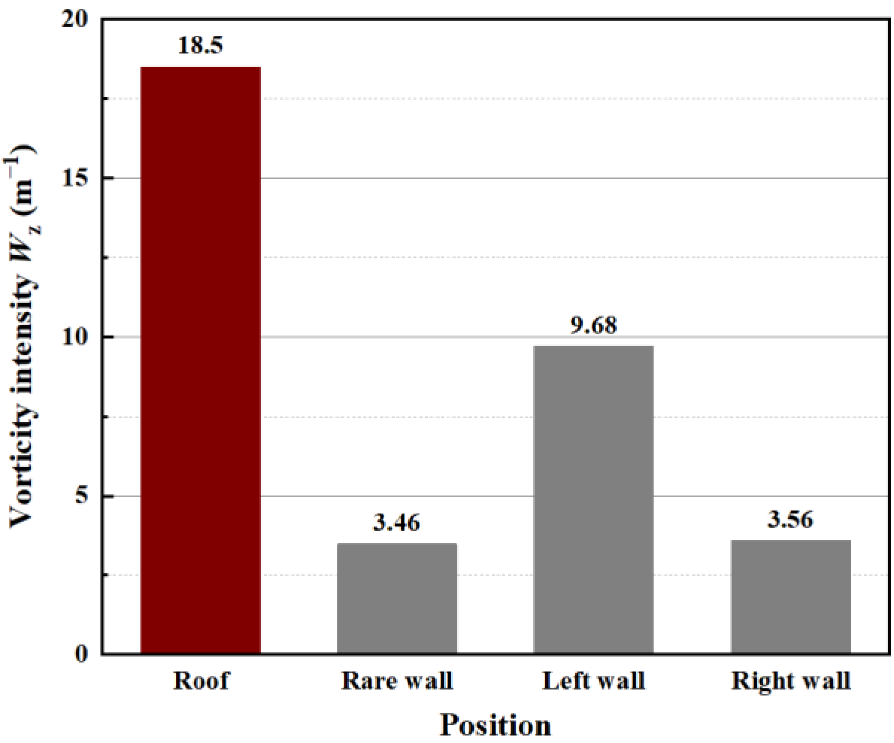

Figure 19. Maximum vorticity intensity of each wall.

3.3. Flow Pattern at the Bell Mouth

Figure 20 shows the pressure distribution at the bell mouth at different time points. It can be seen from the figure that the pressure in the middle of the bell mouth is lower than the sidewall and the flow rate is higher. The distribution of the middle low-pressure zone changes with the rotation of the impeller. However, there is a low-pressure area near the rear wall of the closed sump. The position of the low-pressure area does not change with the rotation of the impeller. When the blade faces the low-pressure area (2/5 T), the pressure is lower relative to other blade positions. At this time, the axial velocity distribution and velocity weighted average angle at the bell mouth also decreased (Figure 21). The flow pattern becomes worse at the inlet of the bell mouth.

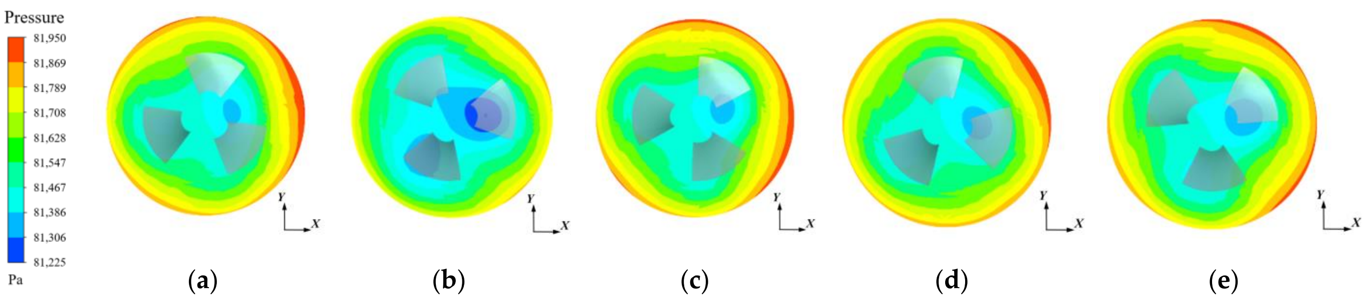

Figure 20. Pressure distribution at the bell mouth at different time points. (**a**) 1/5T. (**b**) 2/5T. (**c**) 3/5T. (**d**) 4/5T. (**e**) T.

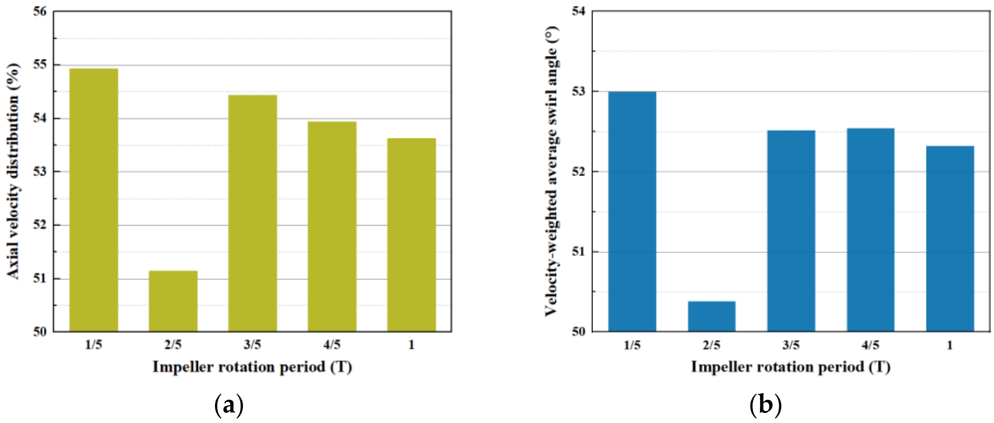

Figure 21. Axial velocity distribution and velocity weighted average angle at bell mouth at different times. (**a**) Axial velocity distribution, (**b**) Velocity weighted average angle.

3.4. RAV Formation Mechanism

To reveal the formation mechanism of RAV, we take the velocity vector distribution on sections S1 and S3 of Figure 14, as shown in Figure 22.

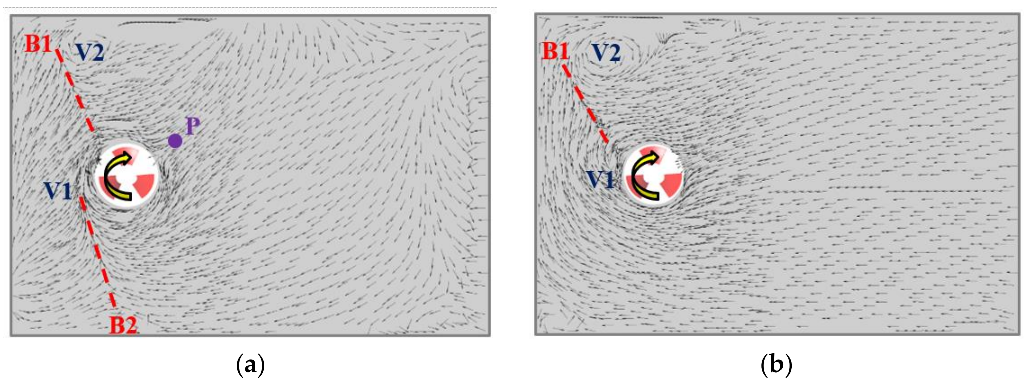

Figure 22. Velocity vector distribution of cross-section at different axial positions. (**a**) S1, (**b**) S3.

According to the previous numerical simulation analysis and experiment, there are two vortex areas on section S1 (near the roof), V1 and V2, respectively. It can be seen from Figure 21a that in section S1, the flow direction is divided into two parts. First, the water flow at the inlet of the closed sump flows to the location of the pump, and second, the water flow on the rear wall flows to the pump. The water flow from the inlet to the pump is separated at point P to form two water flows around the pump. It then intersects with the water flow from the rear wall to the pump at boundaries B1 and B2. Vortices V1 and V2 are formed due to the collision and energy exchange when the water flows meet. In section S3, the flow intersection boundary B2 disappears. The reason is that the position of section S3 close to the bell mouth is greatly affected by the rotation of the impeller, and the flow direction on the left side of the closed sump is consistent.

4. Conclusions

With the development of large-scale and large-flow in the sump of the pumping station, it is very urgent and necessary to broaden the stable operation range and control of a new vortex zone. The CFD unsteady numerical simulation of the working condition of the roof-attached vortex (RAV) is carried out. The predicted location and relative strength of roof wall vortex based on CFD numerical simulation are consistent with the experimental results.

(1) The distribution characteristics of vorticity intensity near the roof at different time points are analyzed. The RAV mainly occurs between the pump device of the closed sump

and the rear wall. The RAV will enter the pump and endanger the safe and stable operation of the pump.

(2) By analyzing the distribution characteristics of the vorticity field on each wall, the variation law of RAV in one period is obtained. The distribution characteristics of the vorticity field near the roof can remain relatively stable, and the vorticity intensity at the vortex core continues to converge and increase with the rotation of the impeller. Comparing the vorticity intensity of the roof, rear wall, and sidewalls, the maximum vorticity intensity at the roof is greater than that of other walls. The roof is more likely to induce vortex.

(3) The formation mechanism of RAV is revealed. The inflow water flow on the roof meets the water flow on the rear wall to form a linear water flow intersection boundary. The flow at the intersection boundary has intense shear action, and vortices are formed at both ends. When the blade faces the low-pressure area (at 2/5 T), the velocity distribution uniformity and velocity weighted average angle at the bell mouth also decrease. The inlet flow pattern at the bell mouth becomes worse.

Author Contributions: CFD numerical simulation, B.Z. and W.J.; Experimental image processing, D.Z.; Data curation, M.Z.; Writing—review & editing, B.Z. and L.C. All authors have read and agreed to the published version of the manuscript.

Funding: This study was supported by the National Natural Science Foundation of China (Grant No.51779214), A Project Funded by the Priority Academic Program Development of Jiangsu Higher Education Institutions (PAPD), and Key Project of Water Resources Technology in Jiangsu Province, China (Grants No. 2019014 and No. 2020027).

Data Availability Statement: The data that support the findings of this study are available from the corresponding author, upon reasonable request.

Conflicts of Interest: The authors declare no conflict of interest.

References

1. Cristofano, L.; Nobili, M.; Caruso, G. Experimental Study on Unstable Free Surface Vortices and Gas Entrainment Onset Conditions. *Exp. Therm. Fluid Sci.* **2014**, *42*, 265–270. [CrossRef]
2. Andersen, A.; Bohr, T.; Stenum, B.; Rasmussen, J.J.; Lautrup, B. The Bathtub Vortex in a Rotating Container. *J. Fluid Mech.* **2006**, *556*, 121–146. [CrossRef]
3. Trefefthen, L.M.; Bilger, P. The Bath-Tub Vortex in the Southern Hemisphere. *Nature* **1965**, *207*, 1084–1085. [CrossRef]
4. Deeny, D.F. An experimental study of air-entraining vortices at pump sumps. *Proc. Inst. Mech. Eng.* **1956**, *170*, 106–116. [CrossRef]
5. Zhang, D.; Jiao, W.; Cheng, L.; Xia, C.; Zhang, B.; Luo, C.; Wang, C. Experimental study on the evolution process of the roof-attached vortex of the closed sump. *Renew. Energy* **2021**, *164*, 1029–1038. [CrossRef]
6. Sarkardeh, H.; Zarrati, A.R.; Jabbari, E.; Roshan, R. Discussion of "prediction of intake vortex risk by nearest neighbors modeling". *J. Hydraul. Eng.* **2012**, *138*, 374–375. [CrossRef]
7. Park, I.; Kim, H.J.; Seong, H.; Rhee, D.S. Experimental studies on surface vortex mitigation using the floating anti-vortex device in sump pumps. *Water* **2018**, *10*, 441. [CrossRef]
8. Van Dyke, M. Swirling Flows Vortex Flow in Nature and Technology. *Science* **1984**, *224*, 730–731. [CrossRef]
9. Sarkardeh, H.; Marosi, M. An analytical model for vortex at vertical intakes. *Water Supply* **2021**, *22*, 31–43. [CrossRef]
10. Song, X.J.; Liu, C. Experimental investigation of pressure pulsation induced by the floor-attached vortex in an axial flow pump. *Adv. Mech. Eng.* **2019**, *11*, 1687814019838708. [CrossRef]
11. Song, X.J.; Liu, C. Experimental investigation of floor-attached vortex effects on the pressure pulsation at the bottom of the axial flow pump sump. *Renew. Energy* **2021**, *145*, 2327–2336. [CrossRef]
12. Song, X.J.; Liu, C. Experimental study of the floor-attached vortices in pump sump using V3V. *Renew. Energy* **2021**, *164*, 752–766. [CrossRef]
13. Kang, W.T.; Yu, K.H.; Lee, S.Y.; Shin, B.R. An investigation of cavitation and suction vortices behavior in pump sump. In Proceedings of the Fluids Engineering Division Summer Meeting, Toronto, ON, Canada, 1–3 August 2022.
14. Pan, Q.; Zhao, R.; Wang, X.; Shi, W.; Zhang, D. LES study of transient behaviour and turbulent characteristics of free-surface and floor-attached vortices in pump sump. *J. Hydraul. Res.* **2018**, *57*, 733–743. [CrossRef]
15. Amin, A.; Kim, B.H.; Kim, C.G.; Lee, Y.H. Numerical Analysis of Vortices Behavior in a Pump Sump. *IOP Conf. Ser. Earth Environ. Sci.* **2019**, *240*, 032020. [CrossRef]
16. Kim, H.J.; Park, S.W.; Rhee, D.S. Effective Height of a Floor Splitter Anti-Vortex Device under Varying Flow Conditions. *Sustainability* **2017**, *9*, 285. [CrossRef]

17. Arocena, V.M.; Abuan, B.E.; Reyes, J.G.T.; Rodgers, P.L.; Danao, L.A.M. Reduction of Entrained Vortices in Submersible Pump Suction Lines Using Numerical Simulations. *Energies* **2021**, *13*, 6136. [CrossRef]
18. Rabe, B.K.; Najafabadi, S.H.G.; Sarkardeh, H. Numerical simulation of air-core vortex at intake. *Curr. Sci.* **2017**, *113*, 141–147. [CrossRef]
19. Tahershamsi, A.; Rahimzadeh, H.; Monshizadeh, M.; Sarkardeh, H. An experimental study on free surface vortex dynamics. *Meccanica* **2018**, *53*, 3269–3277. [CrossRef]
20. Echávez, G.; McCann, E. An experimental study on the free surface vertical vortex. *Exp. Fluids* **2002**, *33*, 414–421. [CrossRef]
21. Cheng, L.; Liu, C.; Zhou, J.; Tang, F.; Yang, H. The study on the flow fields and hydraulic performance in the pump sump. In Proceedings of the 5th Joint ASME/JSME Fluids Engineering Conference, San Diego, CA, USA, 30 July–2 August 2007.
22. Jiao, W.; Cheng, L.; Zhang, D.; Zhang, B.; Su, Y. Investigation of Key Parameters for Hydraulic Optimization of an Inlet Duct Based on a Whole Waterjet Propulsion Pump System. *Trans. FAMENA* **2021**, *45*, 145–162. [CrossRef]
23. Rajendran, V.P.; Patel, V.C. Measurement of vortices in model pump-intake bay by PIV. *J. Hydraul. Eng.* **2000**, *126*, 322–334. [CrossRef]
24. Constantinescu, S.G.; Patel, V.C. Numerical model for simulation of pump-intake flow and vortices. *J. Hydraul. Eng.* **1998**, *124*, 123–134. [CrossRef]
25. Constantinescu, S.G.; Patel, V.C. Role of turbulence model in prediction of pump-bay vortices. *J. Hydraul. Eng.* **2000**, *126*, 387–391. [CrossRef]
26. Choi, J.W.; Choi, Y.D.; Kim, C.G.; Lee, Y.H. Flow Uniformity in a Multi-Intake Pump Sump Model. *J. Mech. Sci. Technol.* **2010**, *24*, 1389–1400. [CrossRef]
27. Okamura, T.; Kamemoto, K.; Matsui, J. CFD Prediction and Model Experiment on Suction Vortices in Pump Sump. In Proceedings of the 9th Asian International Conference on Fluid Machinery, Jeju, Korea, 16–19 October 2007.
28. Li, S.; Silva, J.M.; Lai, Y.; Weber, L.J.; Patel, V.C. Three-dimensional simulation of flows in practical water-pump intakes. *J. Hydroinformatics* **2006**, *8*, 111–124. [CrossRef]
29. Jiao, W.; Cheng, L.; Zhang, D.; Zhang, B.; Su, Y.; Wang, C. Optimal Design of Inlet Passage for Waterjet Propulsion System Based on Flow and Geometric Parameters. *Adv. Mater. Sci. Eng.* **2019**, *10*, 2320981. [CrossRef]
30. Jiao, W.; Cheng, L.; Xu, J.; Wang, C. Numerical Analysis of Two-Phase Flow in the Cavitation Process of a Waterjet Propulsion Pump System. *Processes* **2019**, *7*, 690. [CrossRef]
31. Zhang, D.; Cheng, L.; Li, Y.Y.; Jiao, W.X. The hydraulic performance of twin-screw pump. *J. Hydrodyn.* **2020**, *32*, 605–615. [CrossRef]
32. Hunt, J.C.; Wray, A.A.; Moin, P. Eddies, streams, and convergence zones in turbulent flows. *Stud. Turbul. Using Numer. Simul. Databases* **1988**, *2*, 193–208.
33. Dallmann, U. Topological structures of three-dimensional vortex flow separation. In Proceedings of the 16th Fluid and Plasmadynamics Conference, Danvers, MA, USA, 12–14 July 1983; p. 1735.
34. Liu, C.Q.; Yan, Y.H.; Lu, P. Physics of turbulence generation and sustenance in a boundary layer. *Comput. Fluids* **2014**, *102*, 353–384. [CrossRef]
35. Chong, M.S.; Perry, A.E.; Cantwell, B.J. A general classification of three-dimensional flow fields. *Phys. Fluids A Fluid Dyn.* **1990**, *2*, 765–777. [CrossRef]